

Design of lead-free antiferroelectric $(1 - X)\text{NaNbO}_3 - x\text{SrSnO}_3$ compositions guided by first-principles calculations

Koruza, Jurij; Zhang, Mao Hua; Hadaeghi, Niloofar; Egert, Sonja; Ding, Hui; Zhang, Hongbin; Groszewicz, Pedro B.; Buntkowsky, Gerd; Klein, Andreas

DOI

[10.1021/acs.chemmater.0c03685](https://doi.org/10.1021/acs.chemmater.0c03685)

Publication date

2020

Document Version

Accepted author manuscript

Published in

Chemistry of Materials

Citation (APA)

Koruza, J., Zhang, M. H., Hadaeghi, N., Egert, S., Ding, H., Zhang, H., Groszewicz, P. B., Buntkowsky, G., & Klein, A. (2020). Design of lead-free antiferroelectric $(1 - X)\text{NaNbO}_3 - x\text{SrSnO}_3$ compositions guided by first-principles calculations. *Chemistry of Materials*, 33(1), 266-274. ³
<https://doi.org/10.1021/acs.chemmater.0c03685>

Important note

To cite this publication, please use the final published version (if applicable).
Please check the document version above.

Copyright

Other than for strictly personal use, it is not permitted to download, forward or distribute the text or part of it, without the consent of the author(s) and/or copyright holder(s), unless the work is under an open content license such as Creative Commons.

Takedown policy

Please contact us and provide details if you believe this document breaches copyrights.
We will remove access to the work immediately and investigate your claim.

Design of Lead-Free Antiferroelectric (1-x)NaNbO₃-xSrSnO₃ Compositions Guided by First-Principles Calculations

Mao-Hua Zhang¹, Niloofar Hadaeghi², Sonja Egert³, Hui Ding⁴, Hongbin Zhang², Pedro B. Groszewicz^{3,6}, Gerd Buntkowsky³, Andreas Klein⁵, Jurij Koruza^{1,*}

¹ Department of Materials and Earth Sciences, Nonmetallic Inorganic Materials, Technical University of Darmstadt, Darmstadt, Germany.

² Department of Materials and Earth Sciences, Theory of Magnetic Materials, Technical University of Darmstadt, Darmstadt, Germany.

³ Eduard Zintl Institute for Inorganic and Physical Chemistry, Technical University of Darmstadt, Darmstadt, Germany.

⁴ Department of Materials and Earth Sciences, Advanced Electron Microscopy, Technical University of Darmstadt, Darmstadt, Germany.

⁵ Department of Materials and Earth Sciences, Electronic Structure of Materials, Technical University of Darmstadt, Darmstadt, Germany.

⁶ Department of Radiation Science and Technology, Delft University of Technology, Delft, Netherlands.

*Corresponding author: koruza@ceramics.tu-darmstadt.de

ABSTRACT: Antiferroelectric materials exhibit a unique electric-field-induced phase transition, which enables their use in energy storage, electrocaloric cooling, and non-volatile memory applications. However, in many prototype antiferroelectrics this transition is irreversible, which prevents their implementation. In this work, we demonstrate a general approach to promote the reversibility of this phase transition by targeted modification of the material's local structure. A new NaNbO₃-based composition, namely (1-x)NaNbO₃-xSrSnO₃, was designed with a combination of first-principles calculations and experimental characterization. Our theoretical study predicts stabilization of the antiferroelectric state over the ferroelectric state with an energy difference of 1.4 meV/f.u. when 6.25 mol.% of SrSnO₃ is incorporated into NaNbO₃. A series of samples was prepared using solid state reactions and the structural changes upon SrSnO₃ incorporation were investigated using X-ray diffraction and ²³Na solid-state nuclear magnetic resonance spectroscopy. The results revealed an increase in the unit cell volume and a more disordered, yet less distorted local Na environment, which were related to the stabilization of the antiferroelectric order. The SrSnO₃-modified compositions exhibited well defined double polarization loops and an 8-times higher energy storage density as compared to unmodified NaNbO₃. Our results indicate that this first-principles calculations based approach is of great potential for the design of new antiferroelectric compositions.

Introduction

Oxide-based antiferroelectric perovskites are characterized by the existence of an antipolar phase and a related ferroelectric polar phase with a small free energy difference^{1,2}. This small difference between the antiferroelectric (AFE) and ferroelectric (FE) order enables the phase transformation to be triggered by the application of external stimuli, e.g. electric fields. Given this unique functionality, AFE materials are gaining increasing attention for their potential application in high-energy storage capacitors^{3,4}, which could be used in convertors for renewable energy sources and electric vehicles. Other emerging applications include solid-state electrocaloric cooling^{5,6} and non-volatile random access memories⁷.

The free energy difference can be tailored by chemical composition⁸, microstructure^{9,10}, temperature^{11,12}, and mechanical stress¹³. The phase transformation between AFE and FE phases can be reversible or irreversible in nature. A reversible transition is macroscopically characterized by double polarization hysteresis loops, which is a precondition for the application of these materials. However, there is a limited number of perovskite oxide systems showing such characteristic hysteresis loops at ambient conditions. In many materials that exhibit antipolar ordering, the electric-field-induced phase transition is mostly irreversible (NaNbO_3) or cannot be induced at all (PbZrO_3) at room temperature. The origins of this behavior are not well understood and seem to be related to the free energy difference between the phases and the height of the phase transition energy barrier, which are both defined by the crystallographic structure and chemical bonding.

PbZrO_3 (PZ) was the first compound identified as an AFE material and serves as a model system that has been most thoroughly studied so far^{12,14}. Antiferroelectricity appears upon cooling the material below the structural phase transition at 230 °C, which is accompanied by antiphase rotations of oxygen octahedra along [110] and antiparallel shifts of the Pb^{2+} ions along the pseudocubic $\langle 110 \rangle$ directions. Pure PZ fails to exhibit characteristic double polarization hysteresis loops at room temperature, which is related to the relatively large energy difference (20 meV/f.u.) between AFE and FE phases¹⁵. However, compositionally modified $(\text{Pb,Nb})(\text{Zr,Sn,Ti})\text{O}_3$ ¹⁶ (PNZST) and $(\text{Pb,La})(\text{Zr,Sn,Ti})\text{O}_3$ ¹⁷ (PLZST) material systems allow reversible electric-field induced transitions to be obtained under ambient conditions. Unfortunately, these compositions contain about 60 wt.% of toxic lead. Increasing environmental concerns thus initiated widespread scientific activity in the search for nontoxic replacements of these lead-based materials^{18,19}.

Promising lead-free AFE compositions were found in the group of niobate perovskites^{8, 20-22}. Antiparallel displacements of niobium ions in NaNbO_3 reported earlier²³ made this compound the basis for the recently-discovered group of niobate-based lead-free AFE materials. The irreversibility of the AFE-FE transition in pure NaNbO_3 ^{24, 25} could be altered by the formation of solid solutions with other perovskites^{8, 22, 26}, albeit reversibility was not always achieved at ambient conditions. Recently, exceptionally high energy storage densities could be obtained in some other NaNbO_3 -containing solid solutions²⁷⁻²⁹. However, whether the property enhancement mechanism is related to antiferroelectricity or the relaxor nature is still under debate and the influence of chemical modifications and structural properties of these materials remain to be fully understood.

Despite the lack of complete mechanistic understanding of the crystallographic and electronic structures of AFE, the existing literature provides some basic guidelines for the stabilization of the AFE phase and, hence, achieving reversibility. Earlier investigations suggested that the AFE-FE phase transitions can be tailored by modifying the Goldschmidt tolerance factor. For example, in PZ the A-site substitution with a larger isovalent ion, *e.g.*, Ba^{2+} , stabilizes the FE phase, while A-site substitution with a smaller isovalent ion, *e.g.*, Sr^{2+} , allows for the stabilization of the AFE phase^{30, 31}. Similarly, B-site substitution with a larger ion stabilizes the AFE phase. As demonstrated in the PLZST system, incorporation of more Sn moves the composition deeper into the AFE region of the PbZrO_3 - $\text{Pb}(\text{Zr}_{0.5}\text{Sn}_{0.5})\text{O}_3$ - $\text{Pb}(\text{Zr}_{0.5}\text{Ti}_{0.5})\text{O}_3$ ternary phase diagram, which is accompanied by an increase in the critical field, E_{AF} ³² (electric field required to trigger the field-induced phase transition). This indicates that Sn is an AFE stabilizer when substituting for B-site ions. Shimizu *et al.* demonstrated that these materials design strategies are to some extent also applicable to stabilize the AFE order in NaNbO_3 -based systems, where incorporation of compounds with smaller A-site cations and larger B-site cations resulted in AFE phase stabilization⁸. This result was rationalized by considering a combination of tolerance factor, electronegativity, and polarizability of the ions.

In this work, we have approached the development of new lead-free AFEs using first-principles calculations. The calculated energy differences between individual phases revealed that the stability of the AFE phase in NaNbO_3 increases with the substitution of Sr^{2+} and Sn^{4+} for the A-site and B-site ions, respectively. A series of $(1-x)\text{NaNbO}_3$ - $x\text{SrSnO}_3$ compositions were synthesized and investigated using X-ray diffraction and ²³Na Nuclear Magnetic Resonance (NMR) spectroscopy to reveal the influence of the

substitution on the long-range and local structures. Finally, the new materials were exposed to high electric fields and the existence of well-defined double polarization hysteresis loops and strongly enhanced energy storage density were demonstrated.

EXPERIMENTAL SECTION

First-principles calculations. The density functional theory (DFT) calculations were carried out for pure NaNbO_3 and the solid solution $0.9375\text{NaNbO}_3\text{-}0.0625\text{SrSnO}_3$. The calculations were done using the projector augmented-wave method, as implemented in the VASP code^{33, 34}. For both FE and AFE phases, supercells of 80 atoms are generated and optimized with forces converged to be less than $0.0005 \text{ eV}/\text{\AA}$. The cutoff energy for the plane wave basis is set to be 520 eV for structural relaxation and total energy evaluation, with effective k-mesh of $6 \times 6 \times 3$ in the supercell geometry to ensure good convergence. The exchange-correlation functional is approximated using the generalized gradient approximation (GGA) as parameterized by Perdew–Burke–Ernzerhof (PBE)³⁵. For the NMR calculations, the hyperfine coefficients and chemical shifts are evaluated using a cutoff energy of 650 eV to guarantee good convergence, while the other parameters are kept the same. Specifically, we started with the *Pbcm* (space group 57) and *Pmc2₁* (space group 26) structures for the AFE and FE phases of pure NaNbO_3 , with the experimental lattice parameters (5.504 \AA , 5.570 \AA , 15.517 \AA)³⁶ for the former and (7.8636 \AA , 5.6306 \AA , 5.5483 \AA)³⁷ for the latter. Supercells with 80 atoms correspond to a $\sqrt{2} \times \sqrt{2} \times 1$ supercell for the AFE phase and a $2 \times \sqrt{2} \times \sqrt{2}$ supercell for the FE phase. For the solid solution, one Sr and one Sn atom substitute one Na and one Nb atom out of 16 possible locations for each, respectively, corresponding to a SrSnO_3 composition of 6.25 mol.%. Based on symmetry, Wyckoff position, and the distance between Sr and Sn atoms, we created 10 representative geometries for each of the AFE and FE phases and evaluated the total energies of these structures after full ionic relaxation. The AFE/FE structures with the lowest energies among each set of geometries are selected for the discussions below. Please refer to the Supporting information (Table S1 and Figure S1) for the complete information on such structures, including the corresponding energy values and the Sr–Sn distances.

Sample preparation. The $(1-x)\text{NaNbO}_3\text{-}x\text{SrSnO}_3$ ($x = 0.03\text{--}0.06$ with an interval of 0.01; abbreviated as NN-*x*SS) polycrystalline materials were prepared by solid-state-reaction. High-purity precursors Na_2CO_3 (99.95 %, Alfa Aesar, Germany), SrCO_3 (99.99 %, Alfa Aesar, Germany), SnO_2 (99.90 %, Alfa Aesar, Germany), and orthorhombic Nb_2O_5 (99.50 %, Sinopharm, China) were dried at 200 °C for 8 h and sub-

sequently weighed in a stoichiometric ratio with 1 wt.% excess Na_2CO_3 to compensate for possible evaporation³⁸. All raw materials were homogenized by planetary ball milling using yttria-stabilized zirconia (YSZ) balls in ethanol for 12 h at 250 rpm and then dried at 100 °C. The powder mixtures were calcined at 850 °C for 4 h. The as-calcined powders were subsequently ball milled for 12 h at 250 rpm, dried, and compacted into disks with 10 mm in diameter and 1.5 mm in thickness. The discs were subject to cold isostatic pressing of 200 MPa before sintering at 1360 °C for 2 h using a packing powder with the same composition. The density of the sintered samples was determined by the Archimedes method (Supporting information, Table S2). Scanning electron microscopy (SEM, XL 30 FEG, Philips, Eindhoven, Netherlands) was used to examine the microstructure of the sintered samples, which were ground, polished with diamond paste down to 1.0 μm particle size and thermally etched at 1250 °C for 30 min. Grain size distributions were determined from SEM images (Supporting information, Figures S2 and Figure S3, Table S2).

Structural characterization. The structure was investigated using an X-ray diffractometer (XRD, Bruker AXS D8 Advance, Germany) with $\text{Cu K}\alpha$ radiation. Full-pattern Rietveld analysis was performed with the Jana2006 software package³⁹, using the AFE *P* phase of pure NaNbO_3 as the starting structure (Database ICSD #23239). Details about the refinement process can be found in the Supporting information, Table S3.

^{23}Na NMR spectra were recorded on a Bruker Avance III spectrometer operating with a 7.1 T magnet at a carrier frequency of 79.38 MHz. Four pellets of ceramic NN-0.05SS were cut into cuboids ($2.3 \times 2.3 \times 0.6 \text{ mm}^3$), stacked, and packed into the middle section of a 4 mm zirconia rotor with TiO_2 serving as a filler material. For pure NN, six pellets with dimensions $2.3 \times 2.3 \times 0.4 \text{ mm}^3$ were used⁴⁰. The samples were subjected to magic angle spinning (MAS) at $10 \pm 0.001 \text{ kHz}$ during acquisition and the ^{23}Na chemical shift scale was referenced to the signal of $\text{NaNO}_3(\text{s})$ at $-8.1 \pm 0.1 \text{ ppm}^{41}$. Two-dimensional Satellite Transition Magic Angle Spinning (STMAS) experiments were carried out using a z-filtered sequence⁴². 2128 transients were averaged for each of the 110 increments with a relaxation delay of 1 s. Excitation, mixing, selective 90° and selective 180° pulse lengths were 1.4 μs , 2.1 μs , 21.75 μs , and 40.75 μs , respectively. Line shape simulations were carried out with the program DMFit⁴³.

Electrical measurements. The samples for electrical characterization were cut and ground to a dimension of $1.5 \times 1.5 \times 0.25 \text{ mm}^3$, followed by 400 °C stress-release annealing and sputtering with platinum elec-

trodes to completely cover both $1.5 \times 1.5 \text{ mm}^2$ surfaces. Polarization and strain hysteresis loops were measured with a triangular field amplitude of 16 kV/mm at 1 Hz using a modified Sawyer-Tower circuit and an optical displacement sensor (D63, Philtec Inc., USA). The hysteresis loops in the second cycle are shown. The piezoelectric d_{33} coefficient was measured using a Berlincourt meter (Piezotest PM300, Singapore). An oscillating load of 0.25 N was applied at a frequency of 110 Hz , superimposed on a force bias of 2 N . Temperature-dependent permittivity measurements at a frequency of 10 kHz were performed using an impedance analyzer (4192A LF, Hewlett-Packard, USA) on samples before they were subjected to electric fields.

RESULTS AND DISCUSSION

The AFE phase stabilization in NaNbO_3 by Sr^{2+} and Sn^{4+} substitution was initially investigated using first-principles calculations. In the first step, the stability of the phases in pure NaNbO_3 was calculated. As shown in **Table 1**, the energy difference between the AFE and FE phases is 2.3 meV/f.u. , whereby the FE phase is more stable than the AFE phase. This is in a good agreement with previous reports⁸. The small energy difference corresponds to a temperature change of only 27 K . It is further reduced upon Sr^{2+} and Sn^{4+} substitution and reaches a value of 1.4 meV/f.u. if simply the two most stable calculated AFE and FE structures of NN-0.0625SS are compared (column *a* in **Table 1**). Interestingly, after this substitution the AFE phase is more stable than the FE phase.

However, in real antiferroelectric perovskites, the AFE-FE transition is of a displacive type and, therefore, the atomic configurations in both phases (before and after the transition) correspond to each other. By this we mean that the lattice parameters correspond to each other as if we would rotate the FE structure onto the AFE one before the substitution of Sr and Sn (apart from the distortions, *i.e.*, small rotations or displacements existing in the AFE or FE phases, the atoms in one phase will be mapped onto the same atoms of the other phase). For the Sr/Sn-modified case, the corresponding atomic positions throughout the simulation can be determined using the Wyckoff positions splitting through the phase transition (for Sr modification), followed by geometrical considerations (for Sn modification). Therefore, in order to compare the energies of the AFE and FE phases of NN-0.0625SS, while taking into account the nature of a displacive phase transition, the structures of both phases should have corresponding atomic configurations. Hence, two scenarios were considered (**Table 1**). The scenario in column *b* refers to a situation where the energy of the most stable AFE structure (among ten considered AFE structures) is compared to the one of the corresponding FE structure. In turn, the scenario in column *c* is obtained by choosing the most

stable FE structure among the ten different FE structures, which is then compared to the corresponding AFE structure. The structures of the former scenario are displayed in **Figure 1**. In scenario *b* the energy difference between the most stable AFE structure and the corresponding FE structure is 1.4 meV/f.u., whereby the AFE phase is more stable. Interestingly, in this scenario the corresponding FE structure has the same energy as the FE structure which is the most stable one among the ten different considered FE structures (scenario *c*). In turn, in scenario *c* (**Table 1**) the energy of the corresponding AFE phase is the same as the energy of the most stable AFE structure among the ten different AFE structures. That is, in this case the energy difference is 1.4 meV/f.u. in favor of the AFE phase, too. Therefore, the results suggest that the SrSnO₃ substitution will lead to a more stable AFE phase. Note that a stable AFE phase and the coexistence of a FE phase with a slightly higher energy were previously predicted as a necessary requirement for the existence of AFEs with double polarization loops ^{2, 12}.

Table 1. The energies (per formula unit) and structural parameters for the AFE (*Pbcm*) and FE (*Pmc2₁*) phases of pure and substituted NaNbO₃, as calculated by DFT. Calculations made for a) comparing most stable AFE and FE phases; b) most stable configuration of AFE and the same atomic arrangements of FE phase; c) most stable configuration of FE and the same atomic arrangements of AFE phase.

		NN	NN-0.0625SS		
			a)	b)	c)
AFE phase	E [eV]	-39.08240	-38.60406	-38.60406	-38.60406
	a [Å]	5.564	5.597	5.597	5.597
	b [Å]	5.641	5.600	5.600	5.600
	c [Å]	15.586	15.760	15.760	15.761
	V [Å ³]	489.22	493.94	493.94	493.95
FE phase	E [eV]	-39.08470	-38.60267	-38.60267	-38.60267
	a [Å]	7.798	7.850	7.850	7.850
	b [Å]	5.585	5.612	5.612	5.612
	c [Å]	5.649	5.625	5.624	5.625
	V [Å ³]	246.02	247.78	247.77	247.78
Difference	ΔE [meV]	2.3 (FE more stable)	1.4 (AFE more stable)	1.4 (AFE more stable)	1.4 (AFE more stable)

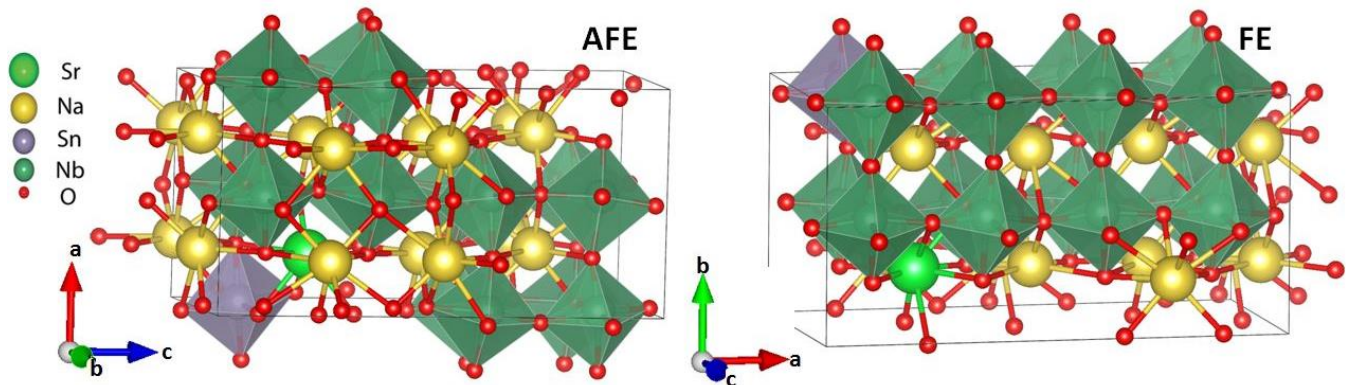


Figure 1. Structures of the most stable AFE configuration of $0.9375\text{NaNbO}_3\text{-}0.0625\text{SrSnO}_3$ and the corresponding FE structure (scenario b in Table 1).

In order to experimentally confirm the phase stability predicted by the DFT calculations, a series of Sr^{2+} and Sn^{4+} substituted NaNbO_3 samples was synthesized using the solid-state reaction method. The XRD patterns in **Figure 2a** confirm the formation of the perovskite phase with the orthorhombic $Pbcm$ structure (details in Figure S4). All samples thus exhibited the P polymorph. We note that a minor amount of a non-perovskite secondary phase was detected in all samples after the calcination treatment. The amount of this phase was too small for reliable identification, but it is likely that its composition is close to SnO_2 . Due to the very small amount, nominal compositions will be used for the following discussion.

The unit cell parameters and cell volume of the samples were determined using the Rietveld refinement method (**Figure 2b**, details in Table S3). Increasing the amount of Sr^{2+} and Sn^{4+} resulted in an increase of the cell parameters a and c , as well as an overall increase in the unit cell volume, which is consistent with the DFT calculations (**Table 1**). This can be explained by the substitution of the smaller Na^+ (1.39 Å; Coordination Number (CN)= 12) and Nb^{5+} (0.64 Å; CN=6) ions by the larger Sr^{2+} (1.44 Å; CN=12) and Sn^{4+} (0.69 Å; CN=6), which is accompanied by a small decrease in the tolerance factor from 0.9671 for NaNbO_3 to 0.9668 for NN-0.05SS.

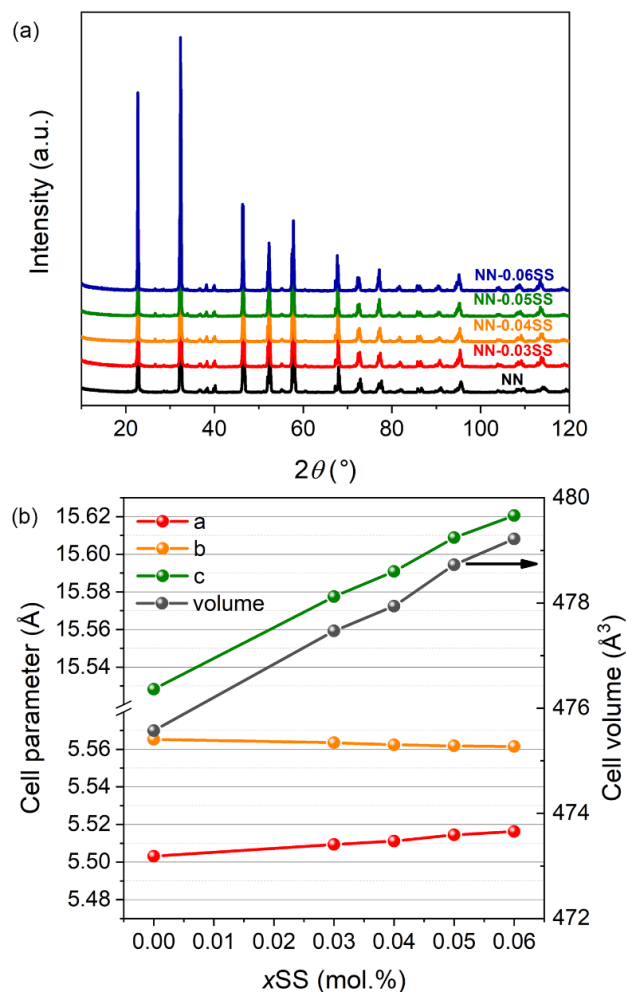


Figure 2. (a) XRD patterns of $(1-x)\text{NaNbO}_3-x\text{SrSnO}_3$ samples. (b) Cell parameters and cell volumes obtained from Rietveld refinements.

^{23}Na solid-state NMR spectroscopy was employed in order to investigate whether the observed AFE stabilization is accompanied by changes to the local structure. **Figure 3a,d** depicts STMAS spectra recorded for pure NaNbO_3 and NN-0.05SS, respectively. Two signals corresponding to sodium sites Na(1) and Na(2) of the NaNbO_3 P polymorph are resolved in the two-dimensional spectrum of **Figure 3a**. No indications for the presence of the Q polymorph are found from the projection along the indirect dimension (δ_1) depicted in **Figure 3b**. Note that these would appear as a shoulder to the Na(1) signal, as first reported by Ashbrook *et al.*⁴⁴ As shown in **Figure 3d**, these two signals are also distinguishable upon 5 mol.% SrSnO_3 substitution, indicating that both sodium sites are still present in the structure. The continuous shape of the signal trace in **Figure 3e** also does not hint at the presence of a polymorph mixture. Furthermore, the positions of both lines do not change significantly. The position of NMR lines is often understood as a “fingerprint” of the structure⁴⁵. However, it should be noted that the presence of small amounts

of a *Q*-like polymorph cannot be completely excluded, due to the broadened Na(1) signal in the δ_1 dimension. The retention of the signals, as well as their positions, indicates that the global structure of the material is preserved upon addition of 5 mol.% SrSnO₃, thereby corroborating the choice of structural models for the DFT calculations. Please note that the absence of the *Q* polymorph was also confirmed by XRD analyses described above.

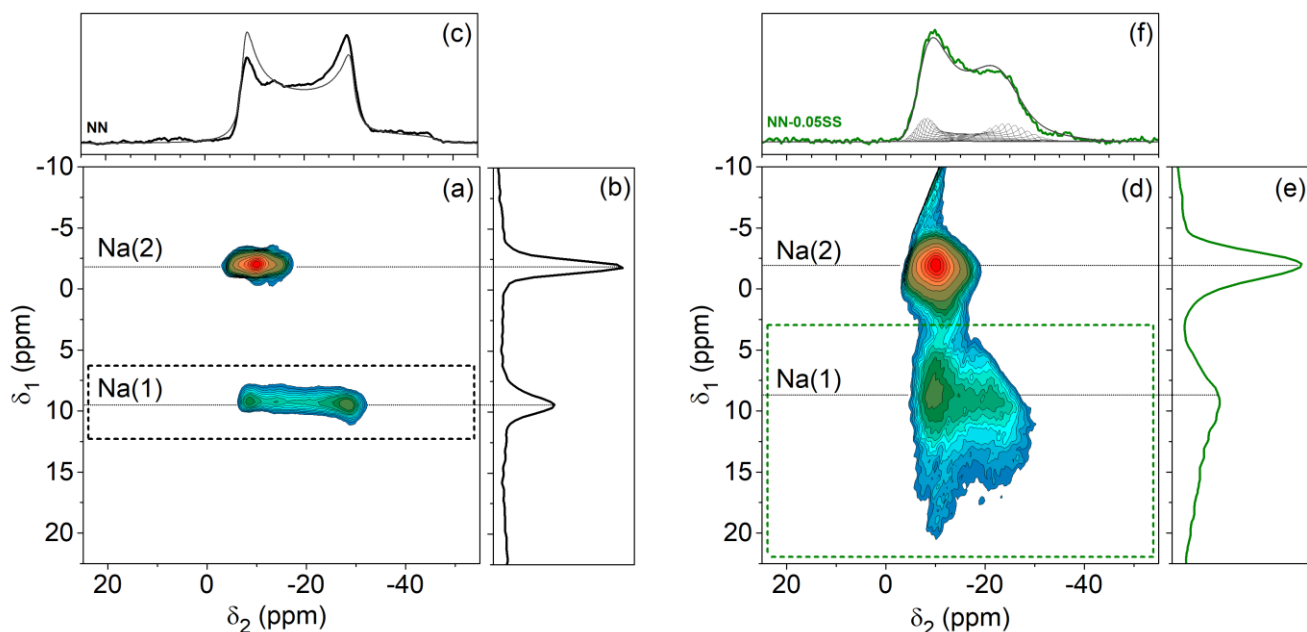


Figure 3. Changes of the local structure upon substitution of 5 mol.% SrSnO₃ into the NaNbO₃ lattice. ²³Na STMAS NMR spectra of (a) pure NaNbO₃ and (d) NN-0.05SS. (b), (e) Summation of the signals along δ_1 . (c), (f) Positive projections of the Na(1) signals (area within the dashed rectangles) along δ_2 with the best achieved line shape simulations, from which NMR parameters and distributions thereof are extracted as described in the text, in grey.

Despite these similarities, it is apparent from **Figure 3** that the width and shape of the signals are affected by the formation of the solid solution. As compared to pure NaNbO₃, both the Na(1) and the Na(2) signals of NN-0.05SS are significantly broadened along the indirect dimension (δ_1), with this effect being more pronounced for the Na(1) site. Besides, the shape of the Na(1) signal changes considerably when compared to that of pure NaNbO₃. The new line shape can be best evaluated by projecting the Na(1) signal along the direct dimension (δ_2) of the spectra (**Figure 3c,f**). While the positive projection for pure NaNbO₃ exhibits a well-defined pattern with maxima at -9 ppm and -29 ppm, and thus matches previously-reported NMR parameters³⁶, the maximum at -29 ppm is washed out in the case of NN-0.05SS. Note that effects of non-uniform excitation of the powder pattern can be observed and are responsible for small deviations between the experimental and fitted lines in the Na(1) projection of pure NaNbO₃ (**Figures 3c** and **S5a** in the Supplementary Information)³⁶, but they cannot account for the line shape of NN-0.05SS in **Figure 3f**.

Line shape analysis shows that the width and the left maximum of the Na(1) projection from NN-0.05SS can be reproduced by a single set of NMR parameters ($C_Q=1.90$ MHz, $\eta=0$; see Figure S5c) with a smaller C_Q value than for pure NN ($C_Q=2.13$ MHz). The decrease in C_Q is also supported by the evaluation of the quadrupolar product (P_Q), which decreases from 2.17 MHz to 2.02 MHz between NN and NN-0.05SS (Figure S6). Despite that, the presence of a plateau instead of a maximum around -29 ppm cannot be well reproduced by a single parameter set. Instead, these changes to the Na(1) signal indicate a distribution of structure-related NMR parameters and thus a broader variation of local environments for Na^+ cations upon the incorporation of SrSnO_3 into the lattice. In a general sense, this can be conceptualized as an increase of disorder in the structure, but analysis of the line shape allows for the identification of the local structural features that are affected.

Hence, we decided to test the effect of the distribution of different NMR parameters individually (δ_{iso} , C_Q , η). A distribution of isotropic chemical shifts δ_{iso} (Figure S5d) results in the same line shape as when Gaussian line broadening is added to the single-parameter fit (Figure S5c). A distribution of η (Figure S5f) results in an attenuation of the left maximum, which is contrary to the line shape observed experimentally. Contrastingly, when a distribution of C_Q is taken into account, the right maximum of the line is significantly attenuated to a plateau (Figure S5e). This effect is a consequence of the increasing line width towards lower frequencies as C_Q increases (for a fixed chemical shift value) in a quadrupole-perturbed NMR line under MAS conditions. In fact, the best fit was achieved by considering a distribution of both C_Q and chemical shift (**Figures 3f** and Figure S5g). This fit resulted in an average C_Q of 1.9(0) MHz and an average chemical shift of -2.(8) ppm, with a distribution width (*i.e.*, standard deviation of a Gaussian distribution) of 0.13(0) MHz and 1.(2) ppm, respectively (**Table 2**). The analysis of the line shape therefore indicates that the modification of NaNbO_3 with SrSnO_3 indeed results in a more disordered, albeit less distorted, local structure for the Na(1) site.

Table 2. Comparison between experimental and computed NMR parameters for the Na(1) site in NaNbO_3 and NN-0.05SS. Values for the latter are described in terms of the average and standard deviation of a distribution (see Table S6 for the complete data).

	Experimental		DFT Calculation	
	NN	NN-0.05SS ^a	NN (AFE)	NN-0.0625SS (AFE)
C_Q (MHz)	2.1(2)	1.9(0)	2.409	2.211
std. deviation	/	0.13(0)	/	0.121
δ (ppm)	-1.(5)	-2.(8)	-1.5 ^b	-1.97
std. deviation	/	1.(2)	/	1.03

a: NMR parameters determined from the best fit to the Na(1) projection (Figure 3c,f).
b: shielding scale referenced with the chemical shift of both Na sites in pure NaNbO_3 (AFE).

This analysis can be extended by a direct comparison of the experimental data to DFT-computed NMR parameters. We have carried out calculations of the chemical shift and electric field gradient (EFG) for both pure NaNbO_3 (as a reference) and NN-0.0625SS (scenario b in **Table 1**). The computed NMR parameters for the Na(1) site are contrasted to the experimental ones in **Table 2**.

Conversion of calculated chemical shielding values to the experimental chemical shift scale spectra requires the use of a reference. On a first instance, pristine NaNbO_3 with an AFE structure suffices as a reference for ^{23}Na chemical shifts. It contains two sodium sites and hence provides two pairs of shielding/shift values for a calibration line. Tables S6 and S7 in the Supplementary Information list the shieldings and chemical shifts found for both sites of NaNbO_3 . The slope of the calibration line deviates from unity, which is a possible consequence of the limited number of sodium environments involved in the calibration procedure. In spite of that, it enables a qualitative analysis of the chemical shift and its distribution, which result from the chemical modification with SrSnO_3 .

The resulting computed chemical shift values for NN-0.0625SS are scattered between -0.3 ppm and -2.8 ppm (**Figure 4a**). From a discrete statistical analysis we determine an average of -1.97 ppm and a standard deviation of 1.03 ppm for the chemical shift of Na(1) (**Table 2**). The order of magnitude for the latter compares well to the fitted spectrum for the case in which only a distribution of chemical shifts is considered in the NMR line shape analysis (Table S4). When both a distribution of C_Q and chemical shifts is taken into account, the best fit was found for a standard deviation of 1.2 ppm for the chemical shift, which matches the calculated value with surprising precision.

The average chemical shift for Na(1) in the NN-0.0625SS model ($\delta = -1.97$ ppm) is found to be more negative than in the reference NN ($\delta = -1.5$ ppm) by 0.5 ppm. The direction of this change is reproduced by the line shape analysis with a distribution of NMR parameters, which requires a chemical shift around -2.8 ppm for a reliable fit. However, the graphical analysis of the signal's centre of gravity (Figure S6), and by extension the isotropic value of the chemical shift and the quadrupolar product resulting thereof (Table S5), indicate a chemical shift of +1.5 ppm for NN-0.05SS. As such small differences in chemical shift by far surpass the precision of the shielding calculation, we refrain from further speculations about this difference.

Further insight can be gained from the evaluation of computed C_Q values. For the Na(1) site of pristine AFE NaNbO_3 , we computed a quadrupolar coupling constant of $C_Q=2.4$ MHz. Although slightly above the experimental value of 2.1 MHz, it allows for a comparison with the SrSnO_3 -modified structure keeping this discrepancy in mind. For the eight Na(1) sites of the NN-0.0625SS supercell, we find a lowered average C_Q value of 2.2 MHz. This trend is in accordance with the experimental values of P_Q and the trend of C_Q values determined from an analysis of the Na(1) line shape (**Table 2**).

Furthermore, we observe that the computed C_Q values for the Na(1) sites of NN-0.0625SS are scattered between 2.0 and 2.4 MHz (**Figure 4b**). An estimate of the standard deviation is found to be equal to 0.121 MHz. This value closely matches the standard deviation of 0.130 MHz which is required for a distribution of C_Q to reproduce the line shape observed in the Na(1) projection of NN-0.05SS (**Figure 3f**). The small number of Na(1) sites sampled by the supercell may increase the uncertainty of the standard deviation by a factor of 2. Nevertheless, the close correspondence between computed and experimental values allows us to interpret them as a measure of the order of magnitude for the distribution of C_Q , and hence the structural disorder which results from the chemical modification in NN-0.05SS.

Next, we attempt an interpretation of the NMR parameters and their distributions in terms of structural parameters predicted from DFT calculations for the Na(1) site. While the chemical shift is often related to average Na-O distances⁴⁶, the EFG magnitude (*i.e.*, C_Q) is a function of the degree of structural distortion of the NaO_{12} cuboctahedral cages⁴⁷. Hence, the distribution of each of these NMR parameters can be related to the Na-O distances determined from DFT calculations. More specifically, the distribution of chemical shifts can be understood in terms of the distribution of average Na-O distances, whereas the distribution of C_Q is related to the variance of Na-O distances in each individual NaO_{12} cuboctahedron.

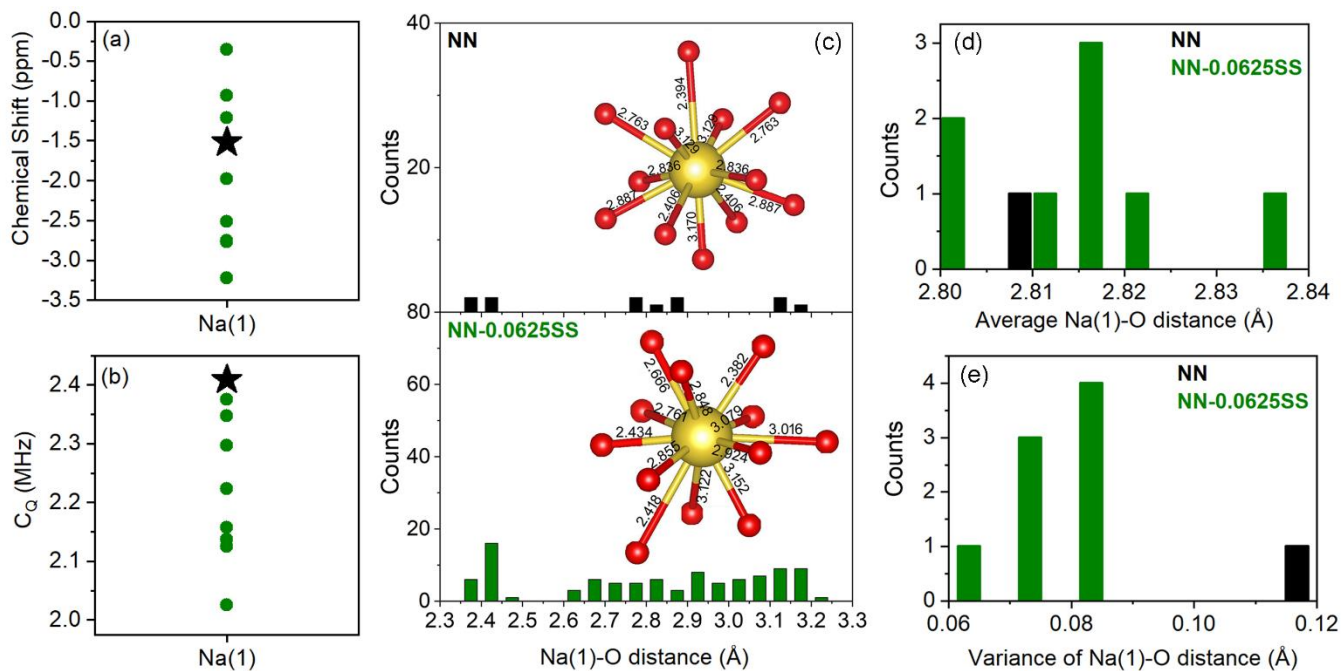


Figure 4. (a) Computed chemical shifts and (b) quadrupolar coupling constants (C_Q) for NN (black) and NN-0.0625SS (green) at all eight Na(1) sites (see Table S6). (c) Calculated Na(1)-O distances for the NaNbO₃ and NaNbO₃-0.0625SS structures of scenario b (Table 1). Insets show the respective NaO₁₂ units of the Na(1) site. (d) Calculated histogram of the average Na-O distances for the Na(1) sites in the structures of NN and NN-0.0625SS. (e) Calculated histogram of the variance of Na(1)-O distances within the NaO₁₂ units for the same site. According to the DFT calculations, Sr occupies the Na(2) site in the supercell of NN-0.0625SS and, hence, there are 8 different Na(1) sites. The average Na(1)-O distance and the variance of Na(1)-O distance for NN-0.0625SS were calculated for these 8 different Na(1) sites.

Figure 4c shows the Na(1)-O distances determined from computed structures of NaNbO₃ and its SrSnO₃-modified counterpart, along with a representative NaO₁₂ unit for the sodium site Na(1). The resulting average Na(1)-O distances for the eight NaO₁₂ units of the NN-0.0625SS supercell, displayed in **Figure 4d**, are spread between 2.804 Å and 2.838 Å, contrasting the singular value of 2.809 Å for all Na(1) cuboctahedra in pure NaNbO₃. The distribution of chemical shifts observed and calculated for the SrSnO₃-modified structure can be understood in terms of this broad variation. In turn, **Figure 4e** shows the variance of Na(1)-O distances for the NaO₁₂ units. While the Na(1)-O variance equals 0.11 for pure NN, eight different values between 0.06 and 0.09 are calculated for the NN-0.0625SS structure model. This is in agreement with the distribution of C_Q found in both the NMR spectrum and the theoretical values. Additionally, the overall decrease of the Na(1)-O variance after the addition of SrSnO₃ indicates a less distorted local structure for the Na(1) site. It can thus be correlated with the decreasing line width of the Na(1) NMR signal as well as the overall lower C_Q values determined from the spectrum and computed for the chemically-modified supercell.

Our analysis demonstrates that the NMR spectra reflect the distribution of local structural features expected from the DFT calculations and, in turn, corroborate the models assumed for the calculation of phase stabilities in SrSnO₃-substituted NaNbO₃. We can speculate that the structural disorder in combination with the lowered structure distortion, which can only be grasped by techniques sensitive to the local scale, affect the electrical properties and the AFE-FE transition in NN-0.05SS.

The influence of the SrSnO₃ substitution and the changed phase stability on the functional properties of NaNbO₃ was evaluated by measuring the dielectric and polarization response. The dielectric properties of the investigated materials are shown in **Figure 5**. The temperature of maximum permittivity at ~370 °C represents the phase transition from *P* to *R* phase^{48, 49} in NaNbO₃. This transition temperature is lower in the investigated SrSnO₃-modified compositions and follows a linear decrease with increasing SrSnO₃ content at a slope of -26.3 ± 0.4 °C/mol.%. While the permittivity maximum decreases with increasing SrSnO₃ content, the value at room temperature increases. The dielectric anomaly observed at ~150 °C for the NaNbO₃ sample (inset of **Figure 5a**) is absent in all the SrSnO₃-modified samples. The dielectric loss shows similar behavior in all the SrSnO₃-modified samples.

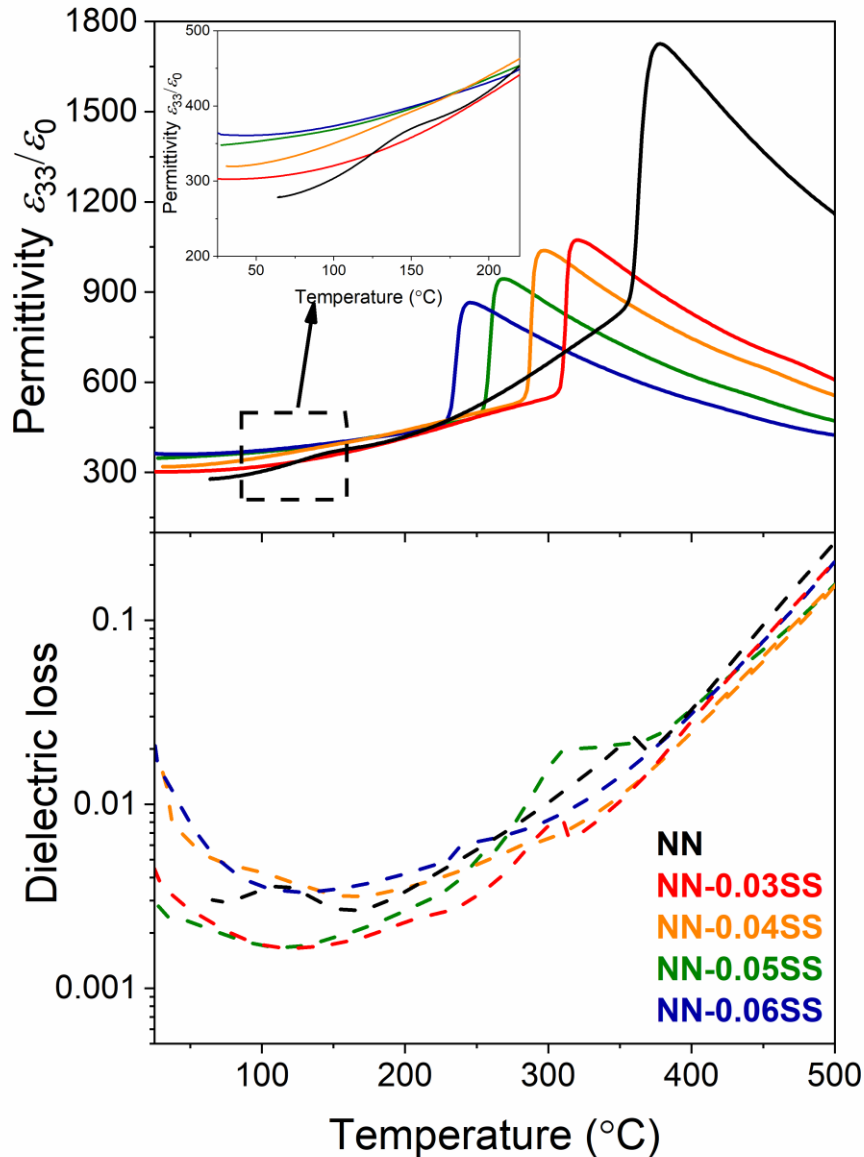


Figure 5. (a) Temperature-dependent dielectric permittivity (solid lines) and (b) dielectric loss (dashed lines) for NN- x SS samples at 10 kHz.

Finally, the NN- x SS samples were subjected to large E -fields with different amplitudes and their polarization, $P(E)$, and strain, $S(E)$, hysteresis loops were compared with those of pure NaNbO_3 as shown in **Figure 6a,b**, respectively. NaNbO_3 exhibits an irreversible electric-field-induced AFE-FE phase transition^{25, 50, 51}, therefore the loops in the second cycle resemble those of a classical ferroelectric. On the other

hand, incorporation of SrSnO₃ considerably changes the polarization and strain behavior and characteristic AFE double polarization loops are observed. The remanent polarization decreases with increasing SrSnO₃ content (**Table 3**), while the critical field E_{AF} increases from 11.6 kV/mm for NaNbO₃ to 12.4 kV/mm, 12.8 kV/mm and 15.0 kV/mm for NN-0.03SS, NN-0.04SS and NN-0.05SS, respectively. We note that the E_{AF} of NN-0.06SS sample was above 15 kV/mm, therefore no saturated loops could be obtained for this composition. The strain hysteresis loops change from butterfly-shaped ferroelectric loops with large negative strain in NaNbO₃ to sprout-shaped loops with minimal negative strain for NN-0.05SS. This behavior confirms the stabilization of the AFE order. The AFE-FE phase transition becomes reversible, meaning that the samples revert into the AFE phase after the electric field is removed. This is confirmed by a decrease of the macroscopic piezoelectric charge coefficient d_{33} with increasing SrSnO₃ content: d_{33} is 35 ± 1 pC/N, 8 ± 1 pC/N, 4 ± 1 pC/N and 2 ± 1 pC/N for NN, NN-0.03SS, NN-0.04SS and NN-0.05SS, respectively (**Table 3**).

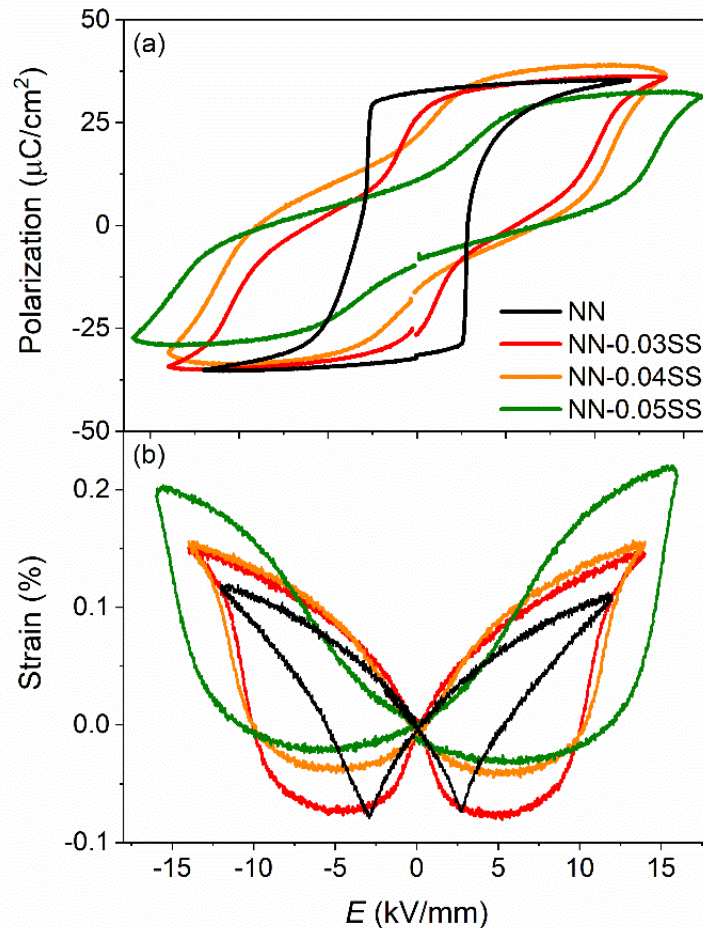


Figure 6. (a) Polarization and (b) strain hysteresis loops of NaNbO₃ and NN- x SS samples in the second cycle (for 1 Hz, room temperature). Hysteresis loops in the first cycle are shown in Figure S7.

Table 3. Electrical properties of NaNbO_3 and $\text{NN-}x\text{SS}$ samples. P_r is the remanent polarization, E_{AF} is the critical field, S_{neg} is the negative strain, d_{33} is the macroscopic piezoelectricity, W_{stor} is the storage energy density, W_{rec} is the recoverable energy density and η is the energy-storage efficiency ($W_{\text{stor}}/W_{\text{rec}}$).

	NN	NN-0.03SS	NN-0.04SS	NN-0.05SS
P_r ($\mu\text{C}/\text{cm}^2$)	32.4	26.3	21.7	11.0
E_{AF} (kV/mm)	11.6	12.4	12.8	15.0
S_{neg} (%)	-0.077	-0.080	-0.043	-0.033
d_{33} (pC/N)	35 ± 1	8 ± 1	4 ± 1	2 ± 1
W_{stor} (J/cm^3)	-	3.52	3.98	4.23
W_{rec} (J/cm^3)	0.12	0.30	0.49	0.90
η (%)	-	8.5	12.2	21.4

From the application point of view, one of the most important parameters for the use of antiferroelectrics for energy storage devices is the energy storage density (W). These values were calculated from the polarization hysteresis loops (**Figure 6a**), revealing an energy storage density of $0.12 \text{ J}/\text{cm}^3$, $0.30 \text{ J}/\text{cm}^3$, $0.49 \text{ J}/\text{cm}^3$ and $0.90 \text{ J}/\text{cm}^3$ for pure NaNbO_3 , NN-0.03SS, NN-0.04SS and NN-0.05SS, respectively. The significantly increased energy storage densities are a consequence of the reversible nature of AFE-FE phase transition in SrSnO_3 -modified samples.

Conclusions

A series of new $(1-x)\text{NaNbO}_3-x\text{SrSnO}_3$ perovskite solid solutions were successfully synthesized using solid state reaction, guided by the predictive power of first-principles calculations. Incorporation of Sr^{2+} and Sn^{4+} into the NaNbO_3 perovskite structure was found to increase the unit cell volume and, at the atomic scale, results in a more disordered, albeit less distorted, local structure for the Na sites. This change triggered the stabilization of the antiferroelectric phase, as evident by the lower free energy, and enabled reversible electric-field-induced AFE-FE transitions. On the macroscopic level this was accompanied by the disappearance of piezoelectricity, appearance of double polarization hysteresis loops, and an 8-times

higher energy storage density of the samples. The presented approach could pave the way for the development of a wide variety of new lead-free antiferroelectric materials for high-energy storage capacitors and non-volatile memories.

Supporting Information.

Figure S1 (Ten representative structures for each of the AFE and FE phases, as calculated by DFT.), Table S1 (Values for energies, Sr-Sn distances, and information about which site (Na(1) or Na(2)) was substituted by Sr.), Table S2 (Density and average grain size of NaNbO_3 and $\text{NaNbO}_3\text{-}x\text{SrSnO}_3$ samples), Figure S2 (SEM images of NaNbO_3 and $\text{NaNbO}_3\text{-}x\text{SrSnO}_3$ samples), Figure S3 (Grain size distributions of NN-0.03SS, NN-0.04SS, NN-0.05SS, and NN-0.06SS samples), Table S3 (Results of the Rietveld refinement of XRD data obtained from crushed and annealed sintered samples), Figure S4 (XRD patterns in the 2θ range of $35.5\text{--}37.5^\circ$, $42.5\text{--}44.2^\circ$ and $54.0\text{--}56.0^\circ$), Figure S5 (Simulated NMR spectra for the Na(1) projections (F2) of NaNbO_3 (a) and NN-0.05SS (b-f) for distribution of different NMR parameters), Table S4 (Parameters for simulation of Na(1) projections (F2) of ^{23}Na STMAS spectra displayed in Figure S5), Figure S6 (Quadrupolar product P_Q determined graphically from the ^{23}Na STMAS NMR spectra), Table S5 (Summary of the analysis of center of gravity from Na(1) STMAS signal), Tables S6, S7 (Summary of computed NMR parameters in NN AFE reference and NN-0.0625SS in scenario b, for Na(1) and Na(2), respectively). Figure S7 (Polarization and strain hysteresis loops of NaNbO_3 and NN- x SS samples in the first cycle, measured at 1 Hz and room temperature).

Corresponding Author

*Jurij Koruza: koruza@ceramics.tu-darmstadt.de;

Author Contributions

All authors have given approval to the final version of the manuscript. J.K., M.-H.Z., and A.K. developed the idea and designed the experiments. N.H. and H.B.Z. performed the first-principles calculations. M.-H.Z. synthesized the samples and characterized electrical properties, crystallographic structures and microstructures. J.K. performed Rietveld refinements. S.E. and P.G. conducted the analysis of the NMR characterization, under the supervision of G.B. H.D. helped with microstructural characterizations. All authors contributed to the preparation of the manuscript.

Notes

The authors declare no competing financial interest.

ACKNOWLEDGMENT

This work was supported by the Hessian State Ministry for Higher Education, Research and the Arts under the LOEWE collaborative project FLAME (Fermi level engineering of antiferroelectric materials for energy storage and insulation systems). P.G. gratefully acknowledges the Dutch Research Council (NWO) for the ECCM Tenure Track funding under project number ECCM.006. Financial support by the Deutsche Forschungsgemeinschaft under Contract BU-911-28-1 is also acknowledged.

REFERENCES

1. Kittel, C., Theory of Antiferroelectric Crystals. *Phys. Rev.* **1951**, 82, (5), 729-732.
2. Rabe, K. M., Antiferroelectricity in Oxides: A Reexamination. In *Functional Metal Oxides*, 2013; pp 221-244.
3. Liu, Z.; Lu, T.; Ye, J.; Wang, G.; Dong, X.; Withers, R.; Liu, Y., Antiferroelectrics for Energy Storage Applications: a Review. *Adv. Mater. Technol.* **2018**, 3, (9), 1800111.
4. Hao, X., A review on the dielectric materials for high energy-storage application. *J. Adv. Dielectr.* **2013**, 03, (01), 1330001.
5. Mischenko, A. S.; Zhang, Q.; Scott, J. F.; Whatmore, R. W.; Mathur, N. D., Giant Electrocaloric Effect in Thin-Film $\text{PbZr}_{0.95}\text{Ti}_{0.05}\text{O}_3$. *Science* **2006**, 311, (5765), 1270.
6. Novak, N.; Weyland, F.; Patel, S.; Guo, H.; Tan, X.; Rödel, J.; Koruza, J., Interplay of conventional with inverse electrocaloric response in $(\text{Pb,Nb})(\text{Zr,Sn,Ti})\text{O}_3$ antiferroelectric materials. *Phy. Rev. B* **2018**, 97, (9), 094113.
7. Vopson, M. M.; Caruntu, G.; Tan, X., Polarization reversal and memory effect in anti-ferroelectric materials. *Scr. Mater.* **2017**, 128, 61-64.
8. Shimizu, H.; Guo, H.; Reyes-Lillo, S. E.; Mizuno, Y.; Rabe, K. M.; Randall, C. A., Lead-free antiferroelectric: $x\text{CaZrO}_3-(1-x)\text{NaNbO}_3$ system ($0 \leq x \leq 0.10$). *Dalton Trans.* **2015**, 44, (23), 10763-10772.
9. Koruza, J.; Groszewicz, P.; Breitzke, H.; Buntkowsky, G.; Rojac, T.; Malič, B., Grain-size-induced ferroelectricity in NaNbO_3 . *Acta Mater.* **2017**, 126, 77-85.
10. Shiratori, Y.; Magrez, A.; Dornseiffer, J.; Haegel, F.-H.; Pithan, C.; Waser, R., Polymorphism in Micro-, Submicro-, and Nanocrystalline NaNbO_3 . *J. Phys. Chem. B* **2005**, 109, (43), 20122-20130.
11. Dai, Z.; Yao, X.; Xu, Z.; Feng, Y.; Wang, J., Properties of $\text{PbLa}(\text{Zr,Sn,Ti})\text{O}_3$ ceramics near ferroelectric-antiferroelectric phase boundary. *Chin. Sci. Bull.* **2006**, 51, (8), 1000-1004.
12. Shirane, G.; Sawaguchi, E.; Takagi, Y., Dielectric Properties of Lead Zirconate. *Phys. Rev.* **1951**, 84, (3), 476-481.
13. Saito, T.; Adachi, H.; Wada, T.; Adachi, H., Pulsed-Laser Deposition of Ferroelectric NaNbO_3 Thin Films. *Jpn. J. App. Phys.* **2005**, 44, (9B), 6969-6972.

14. Sawaguchi, E.; Maniwa, H.; Hoshino, S., Antiferroelectric Structure of Lead Zirconate. *Phys. Rev.* **1951**, 83, (5), 1078-1078.
15. Singh, D. J., Structure and energetics of antiferroelectric PbZrO₃. *Phy. Rev. B* **1995**, 52, (17), 12559-12563.
16. He, H.; Tan, X., A Comparative Study of the Structure and Properties of Sn-Modified Lead Zirconate Titanate Ferroelectric and Antiferroelectric Ceramics. *J. Am. Ceram. Soc.* **2007**, 90, (7), 2090-2094.
17. Berlincourt, D., Transducers Using Forced Transitions Between Ferroelectric and Antiferroelectric States. *IEEE Trans. Son. Ultrason.* **1966**, 13, (4), 116-124.
18. Rödel, J.; Li, J.-F., Lead-free piezoceramics: Status and perspectives. *MRS Bull.* **2018**, 43, (8), 576-580.
19. Tan, X.; Ma, C.; Frederick, J.; Beckman, S.; Webber, K. G., The Antiferroelectric ↔ Ferroelectric Phase Transition in Lead-Containing and Lead-Free Perovskite Ceramics. *J. Am. Ceram. Soc.* **2011**, 94, (12), 4091-4107.
20. Zhao, L.; Liu, Q.; Gao, J.; Zhang, S.; Li, J.-F., Lead-Free Antiferroelectric Silver Niobate Tantalate with High Energy Storage Performance. *Adv. Mater.* **2017**, 29, (31), 1701824.
21. Gao, J.; Zhao, L.; Liu, Q.; Wang, X.; Zhang, S.; Li, J.-F., Antiferroelectric-ferroelectric phase transition in lead-free AgNbO₃ ceramics for energy storage applications. *J. Am. Ceram. Soc.* **2018**, 101, (12), 5443-5450.
22. Guo, H.; Shimizu, H.; Mizuno, Y.; Randall, C. A., Domain configuration changes under electric field-induced antiferroelectric-ferroelectric phase transitions in NaNbO₃-based ceramics. *J. Appl. Phys.* **2015**, 118, (5), 054102.
23. Vousden, P., The structure of ferroelectric sodium niobate at room temperature. *Acta Crystallogr.* **1951**, 4, (6), 545-551.
24. Cross, L. E.; Nicholson, B. J., The optical and electrical properties of single crystals of sodium niobate. *Lond. Edinb. Dubl. Phil. Mag.* **1955**, 46, (376), 453-466.
25. Zhang, M.-H.; Fulanović, L.; Egert, S.; Ding, H.; Groszewicz, P. B.; Kleebe, H.-J.; Molina-Luna, L.; Koruza, J., Electric-Field-Induced Antiferroelectric to Ferroelectric Phase Transition in Polycrystalline NaNbO₃. *Acta Mater.* **2020**, 200, 127-135.
26. Ye, J.; Wang, G.; Chen, X.; Cao, F.; Dong, X., Enhanced antiferroelectricity and double hysteresis loop observed in lead-free (1-x)NaNbO₃-xCaSnO₃ ceramics. *Appl. Phys. Lett.* **2019**, 114, (12), 122901.
27. Qi, H.; Zuo, R.; Xie, A.; Tian, A.; Fu, J.; Zhang, Y.; Zhang, S., Ultrahigh Energy-Storage Density in NaNbO₃-Based Lead-Free Relaxor Antiferroelectric Ceramics with Nanoscale Domains. *Adv. Funct. Mater.* **2019**, 29, (35), 1903877.
28. Ye, J.; Wang, G.; Zhou, M.; Liu, N.; Chen, X.; Li, S.; Cao, F.; Dong, X., Excellent comprehensive energy storage properties of novel lead-free NaNbO₃-based ceramics for dielectric capacitor applications. *J. Mater. Chem. C* **2019**, 7, (19), 5639-5645.
29. Shi, J.; Chen, X.; Li, X.; Sun, J.; Sun, C.; Pang, F.; Zhou, H., Realizing ultrahigh recoverable energy density and superior charge-discharge performance in NaNbO₃-based lead-free ceramics via a local random field strategy. *J. Mater. Chem. C* **2020**, 8, (11), 3784-3794.
30. Park, S.-E.; Markowski, K.; Yoshikawa, S.; Cross, L. E., Effect on Electrical Properties of Barium and Strontium Additions in the Lead Lanthanum Zirconate Stannate Titanate System. *J. Am. Ceram. Soc.* **1997**, 80, (2), 407-412.
31. Sawaguchi, E.; Kittaka, T., Antiferroelectricity and Ferroelectricity in Lead Zirconate. *J. Phys. Soc. Jpn.* **1952**, 7, (3), 336-337.
32. Markowski, K.; Park, S.-E.; Yoshikawa, S.; Cross, L. E., Effect of Compositional Variations in the Lead Lanthanum Zirconate Stannate Titanate System on Electrical Properties. *J. Am. Ceram. Soc.* **1996**, 79, (12), 3297-3304.

33. Kresse, G.; Furthmüller, J., Efficient iterative schemes for ab initio total-energy calculations using a plane-wave basis set. *Phys. Rev. B* **1996**, 54, (16), 11169-11186.
34. Kresse, G.; Furthmüller, J., Efficiency of ab-initio total energy calculations for metals and semiconductors using a plane-wave basis set. *Comput. Mater. Sci.* **1996**, 6, (1), 15-50.
35. Perdew, J. P.; Burke, K.; Ernzerhof, M., Generalized Gradient Approximation Made Simple. *Phys. Rev. Lett.* **1996**, 77, (18), 3865-3868.
36. Johnston, K. E.; Tang, C. C.; Parker, J. E.; Knight, K. S.; Lightfoot, P.; Ashbrook, S. E., The Polar Phase of NaNbO₃: A Combined Study by Powder Diffraction, Solid-State NMR, and First-Principles Calculations. *J. Am. Chem. Soc.* **2010**, 132, (25), 8732-8746.
37. Shanker, V.; Samal, S. L.; Pradhan, G. K.; Narayana, C.; Ganguli, A. K., Nanocrystalline NaNbO₃ and NaTaO₃: Rietveld studies, Raman spectroscopy and dielectric properties. *Solid State Sci.* **2009**, 11, (2), 562-569.
38. Popovič, A.; Bencze, L.; Koruza, J.; Malič, B., Vapour pressure and mixing thermodynamic properties of the KNbO₃–NaNbO₃ system. *RSC Advances* **2015**, 5, (93), 76249-76256.
39. Petříček, V.; Dušek, M.; Palatinus, L., Crystallographic Computing System JANA2006: General features. *Cryst. Mater.* **2014**, 229, (5), 345.
40. Egert, S.; Zhang, M.-H.; Koruza, J.; Groszewicz, P. B.; Buntkowsky, G., ²³Na NMR Spectroscopic Quantification of the Antiferroelectric–Ferroelectric Phase Coexistence in Sodium Niobate. *J. Phys. Chem. C* **2020**, 124, (43), 23852-23858.
41. Skibsted, J.; Nielsen, N. C.; Bildsøe, H.; Jakobsen, H. J., Satellite transitions in MAS NMR spectra of quadrupolar nuclei. *J. Magn. Reson.* **1991**, 95, (1), 88-117.
42. Kwak, H.-T.; Gan, Z., Double-quantum filtered STMAS. *J. Magn. Reson.* **2003**, 164, (2), 369-372.
43. Massiot, D.; Fayon, F.; Capron, M.; King, I.; Le Calvé S.; Alonso, B.; Durand, J.-O.; Bujoli, B.; Gan, Z.; Hoatson, G., Modelling one- and two-dimensional solid-state NMR spectra. *Magn. Reson. Chem.* **2002**, 40, (1), 70-76.
44. Ashbrook, S. E.; Le Pollès, L.; Gautier, R.; Pickard, C. J.; Walton, R. I., ²³Na multiple-quantum MAS NMR of the perovskites NaNbO₃ and NaTaO₃. *Phys. Chem. Chem. Phys.* **2006**, 8, (29), 3423-3431.
45. Dec, S. F.; Davis, M. F.; Maciel, G. E.; Bronnimann, C. E.; Fitzgerald, J. J.; Han, S. S., Solid-state multinuclear NMR studies of ferroelectric, piezoelectric, and related materials. *Inorg. Chem.* **1993**, 32, (6), 955-959.
46. George, A. M.; Stebbins, J. F., High-temperature ²³Na MAS NMR data for albite: Comparison to chemical-shift models. *Am. Mineral.* **1995**, 80, (9-10), 878-884.
47. Groszewicz, P. B.; Gröting, M.; Breitzke, H.; Jo, W.; Albe, K.; Buntkowsky, G.; Rödel, J., Reconciling Local Structure Disorder and the Relaxor State in (Bi_{1/2}Na_{1/2})TiO₃-BaTiO₃. *Sci. Rep.* **2016**, 6, (1), 31739.
48. Megaw, H. D., The seven phases of sodium niobate. *Ferroelectrics* **1974**, 7, (1), 87-89.
49. Raevskaya, S. I.; Malitskaya, M. A.; Chou, C.-C.; Lutokhin, A. G.; Raevski, I. P.; Titov, V. V., Dielectric and Pyroelectric Properties of Sodium Niobate Ceramics Containing Inclusions of Ferroelectric Q Phase. *Phys. Status Solidi A* **2019**, 216, (22), 1800972.
50. Ulinzheev, A. V.; Leiderman, A. V.; Smotrakov, V. G.; Topolov, V. Y.; Fesenko, O. E., Phase transitions induced in NaNbO₃ crystals by varying the direction of an external electric field. *Phys. Solid State* **1997**, 39, (6), 972-974.
51. Zhelnova, O. A.; Fesenko, O. E., Phase transitions and twinning in NaNbO₃ crystals. *Ferroelectrics* **1987**, 75, (1), 469-475.

Table of Contents

